

## Characterisation of scheelite $\text{LaW}_{0.16}\text{Nb}_{0.84}\text{O}_{4.08}$ ion conductor by combined synchrotron techniques: structure, W oxidation state and interdiffusion

Giovanna Canu <sup>\*a</sup>, Francesco Giannici <sup>b</sup>, Alessandro Chiara <sup>b</sup>, Giorgia Confalonieri <sup>c</sup>, Alessandro Longo <sup>d,e</sup>, Maria Teresa Buscaglia <sup>a</sup>, Monica Dapiaggi <sup>f</sup>, Vincenzo Buscaglia <sup>a</sup>, Antonino Martorana <sup>b</sup>

<sup>a</sup> CNR-ICMATE – Institute of Condensed Matter Chemistry and Technologies for Energy, via De Marini 6, 16149 Genova, Italy

<sup>b</sup> Dipartimento di Fisica e Chimica “Emilio Segrè”, University of Palermo, viale delle Scienze, 90128 Palermo, Italy

<sup>c</sup> Dipartimento di Scienze Chimiche e Geologiche (DSCG), University of Modena and Reggio Emilia, via Giuseppe Campi 103, 41125 Modena, Italy

<sup>d</sup> ISMN-CNR - Istituto per lo Studio dei Materiali Nanostrutturati, Via Ugo La Malfa, 153, 90146 Palermo, Italy

<sup>e</sup> European Synchrotron Radiation Facility, 71, avenue des Martyrs, Grenoble, F-38000, France

<sup>f</sup> Dipartimento di Scienze della Terra, University of Milano, via Botticelli 23, 20133 Milano, Italy

### Abstract

Scheelite-type materials such as  $\text{LaNbO}_4$  are increasingly attracting attention as a possible alternative to the most common fluorite and perovskite structure as ion conductors. However, they are much less used and investigated. The introduction of tungsten in lanthanum orthoniobate leads to conduction properties that are compatible with oxygen ion conductivity. In this paper, we studied the effect of the introduction of tungsten in the  $\text{LaNbO}_4$  structure. High resolution X-ray diffraction showed that in  $\text{LaW}_x\text{Nb}_{1-x}\text{O}_{4+x/2}$  with  $x = 0.16$  the monoclinic distortion is largely suppressed and the tetragonal phase is predominant at room temperature. By XANES/EXAFS we proved that tungsten is in its 6+ valence state and no  $\text{W}^{5+}$  was detected. With X-ray microspectroscopy, we studied in detail with a submicrometre-probe the interdiffusion and degradation processes taking place between the material and LSM, a common electrode material, during their long-term contact at high temperatures.

**Keywords:** scheelite; electrolyte; solid-oxide fuel cells; XANES; LSM; chemical compatibility

## 1. Introduction

The most common ceramic ionic conductors for use as electrolytes in Solid Oxide Fuel Cells (SOFCs) belong to two types of structures: the fluorite and perovskite crystal structure. Well known examples of oxygen ion conductors with fluorite structure are yttria-stabilised zirconia (YSZ) and ceria-based materials, such as Sm:CeO<sub>2</sub> or Gd:CeO<sub>2</sub> [1,2], while (Sr,Mg)-doped lanthanum gallate and BaCe<sub>1-x</sub>Y<sub>x</sub>O<sub>3</sub> (BCY) possess a perovskite structure and are respectively an oxide ion and a proton conductor [3,4].

More recently, materials with scheelite structure have shown ionic conductivity as well, attracting an increasing interest of researchers. Large attention was devoted to lanthanum niobate-based ceramics [4-7] after the work of Norby and Hausgrud [8] on acceptor-doped LaNbO<sub>4</sub> as a proton conductor. However, other scheelite-type materials, such as CeNbO<sub>4+δ</sub> [9], PbWO<sub>4</sub>-based ceramics [10] and MMoO<sub>4</sub>, M = Ca, Sr, Ba [11,12], were recently investigated for their oxide ion conductivity properties.

The moderate proton conductivity of LaNbO<sub>4</sub>-based materials, together with the presence of a phase transition between the low temperature fergusonite structure and the high temperature scheelite structure around the possible temperature of operation of a fuel cell and the difficulties of increasing the amount of dopants and thus proton conductivity, somehow hindered its development as an electrolyte material for SOFCs. The partial substitution of niobium with tungsten in the lattice, with the formation of LaW<sub>x</sub>Nb<sub>1-x</sub>O<sub>4+x/2</sub>, showed, instead, conduction properties compatible with pure oxygen ion conductivity in a wide range of temperatures and gas atmospheres [13-15]. In particular, for the composition for x = 0.16 we measured a total conductivity at 800 °C of 1.4·10<sup>-3</sup> S·cm<sup>-1</sup> in air and 2.5·10<sup>-3</sup> S·cm<sup>-1</sup> in wet hydrogen [13]. With increasing amount of tungsten substitution, a marked increase of tetragonality was observed in the X-ray diffraction pattern at room temperature of LaW<sub>x</sub>Nb<sub>1-x</sub>O<sub>4+x/2</sub> [16,17], until the fergusonite monoclinic distortion typical of neat LaNbO<sub>4</sub> is completely suppressed for a W content of x ≈ 0.16, as shown in a recent updated phase diagram [17]. Nevertheless, some contrasting results on the actual average structure of this composition, either monoclinic or tetragonal, have been reported [13,14,16,18], possibly related to sensitivity to processing or deviation from stoichiometry. In scheelite, oxygen ion conductivity occurs via interstitial oxide ions, instead of the more common mechanisms involving oxygen vacancies; a few studies reported on the mechanisms of migration of oxide ions in LaW<sub>x</sub>Nb<sub>1-x</sub>O<sub>4+x/2</sub> [18,19]. Beside this, this material is still relatively little known.

The aim of this work is to investigate the effect of the introduction of tungsten on lanthanum niobate on its structure and, with the perspective of its use as an electrolyte for SOFCs, to investigate in detail how the presence of tungsten affects the chemical compatibility of this material with a potential cathode material, such as  $\text{La}_{1-x}\text{Sr}_x\text{MnO}_{3-\delta}$ , LSM, previously demonstrated to show extensive compatibility with both  $\text{LaNbO}_4$  (pure or Ca-doped) [20,21] [22] and  $\text{LaW}_{0.16}\text{Nb}_{0.84}\text{O}_{4.08}$  [13]. Thus,  $\text{LaW}_x\text{Nb}_{1-x}\text{O}_{4+x/2}$  ceramics with  $x = 0.16$  were characterised with high resolution techniques available at the European Synchrotron Radiation Facility (ESRF) – Grenoble, such as high resolution X-ray powder diffraction (XRPD), X-ray absorption near-edge structure (XANES) and Extended X-ray Absorption Fine Structure (EXAFS) on the ceramics and X-ray microspectroscopy on a model electrolyte/cathode interface. The latter method was employed instead of more common methods, such as X-ray diffraction on powder mixtures and SEM/EDS on electrode/electrolyte interfaces, because it combines information on the spatial distribution of cations, using X-ray fluorescence maps, with chemical and structural information about the environment of atomic species, using space-resolved micro-XANES in selected spots [23-25].

## 2. Materials and methods

### 2.1 Samples preparation: bulk LWN ceramic and LSM/LWN bilayer

Highly dense  $\text{LaW}_x\text{Nb}_{1-x}\text{O}_{4+x/2}$  ceramics with  $x = 0.16$ , hereby denoted as LWN, were prepared according to the procedure described in Ref. [13]. Details on their basic characterisation together with electrochemical properties can be found in the same reference. We recall here that with laboratory X-ray powder diffraction (XRPD) the ceramic structure resulted tetragonal; moreover, EDS confirmed cation content close to stoichiometric values, i.e. La = 98 at%, Nb = 85 at%, and W = 17 at%; no secondary phases were detected. The resulting cylindrical pellets were cut into disks of about 10 mm diameter and 1 mm thickness for characterisation or further processing.

For both high resolution XRPD and EXAFS measurements, the ceramics were manually ground before the measurements. For the study of the interface, a bilayer with a sharp interface between LWN and  $\text{La}_{0.8}\text{Sr}_{0.2}\text{MnO}_3$  (LSM) was prepared as follows: an LWN ceramic disk was mechanically polished, surrounded with LSM powder ( $\text{La}_{0.8}\text{Sr}_{0.2}\text{MnO}_3$ , Sigma-Aldrich, >99%) and uniaxially pressed at 7 tons in a 1-inch die. After pressing, the bilayer diffusion couple was annealed at 1150 °C for 72 h. After the thermal treatment, the sample was embedded in resin,

cut to expose the interface, and the cross-section was mechanically polished with SiC emery paper and diamond paste, down to 1  $\mu\text{m}$  nominal roughness.

*2.2 X-ray powder diffraction (XRPD).* High-energy, high resolution XRPD data were obtained at the beamline ID22 at ESRF (Grenoble, France) [26]. The beam wavelength ( $\lambda = 0.294932 \text{ \AA}$ ) was set by a channel-cut Si(111) crystal monochromator. The sample was ground and placed in a borosilicate glass capillary. Data were collected in Debye-Scherrer geometry using a bank of nine detectors, each preceded by a Si(111) crystal analyser. Patterns were collected at temperatures of 100 K and 300 K using an Oxford Cryosystems cold-nitrogen-gas blower.

*2.3 X-ray Absorption Near-Edge Spectroscopy (XANES) and Extended X-ray Absorption Fine Structure (EXAFS).* X-ray absorption spectra at the W  $L_3$ -edge (10.2 keV) on LWN ground powder were acquired in transmission mode at 80 K at the BM26A beamline of ESRF (Grenoble, France). The XANES spectra were modelled with FDMNES [27]. The EXAFS data were modelled with Viper [28] using theoretical amplitude and data from FEFF9 [29].

*2.4 X-ray Microspectroscopy.* Scanning X-ray microscopy measurements on the LSM/LWN bilayers were carried out at the SXM-II end station of the ID21 beamline of ESRF (Grenoble, France) [30]. A focused monochromatic X-ray microbeam with a spot size of  $450 \times 750 \text{ nm}^2$  (H x V) was used to scan the exposed interface, exciting fluorescence radiation from the sample. The energies available at this beamline are comprised in the 2-9 keV range. The microXRF (X-ray Fluorescence) maps and microXAS (X-ray Absorption Spectroscopy) spectra at the Mn K-edge (6.54 keV) were collected using a SDD detector. Details on the experimental setup and data analysis, including the conventional definition of the position of the interface, are reported in previous papers [23-25].

### 3. Results and discussion

#### 3.1 X-ray powder diffraction

The parent phase  $\text{LaNbO}_4$  at room temperature has a fergusonite structure and undergoes a phase transition to the scheelite structure around 770 K [31]. The series of  $\text{LaW}_x\text{Nb}_{1-x}\text{O}_{4+x/2}$  ceramics with  $x = 0.11\text{-}0.22$  is known [16] to have a room temperature structure going from monoclinic (fergusonite-type, as  $\text{LaNbO}_4$ ) to tetragonal (scheelite-type) with increasing amount of tungsten substitution. However, from the literature it is not clear how large the  $x$  value must be until the monoclinic phase transition is suppressed; the composition  $x = 0.16$  has been reported in the literature as being either monoclinic or tetragonal [13,14,16,18]. A recent

phase diagram shows that at room temperature this composition is very close to the fergusonite-scheelite transition [17]. These discrepancies are possibly related to sensitivity to processing and slight inhomogeneities or deviation from stoichiometry.

The diffraction peaks observed at 300 K in the high-resolution XRPD pattern (**Figure 1**) point to the existence of a dominant tetragonal phase, according to the most recent phase diagram [17], and a minor amount of monoclinic phase. The monoclinic phase, indeed, is assumed to be responsible for the broadening of most of the tetragonal peaks near their base whereas the FWHM is rather small. The observation of a broadening rather than a splitting is indicative of a reduced monoclinic distortion in comparison to the compositions with lower x values. When XRPD patterns are collected with an ordinary diffractometer, the convolution with the instrumental broadening produces a more homogeneous peak broadening effect and a pattern typical of the purely tetragonal phase [13]. Additional peaks related to an incommensurate modulated superstructure can also be observed according to previous reports [16,17].

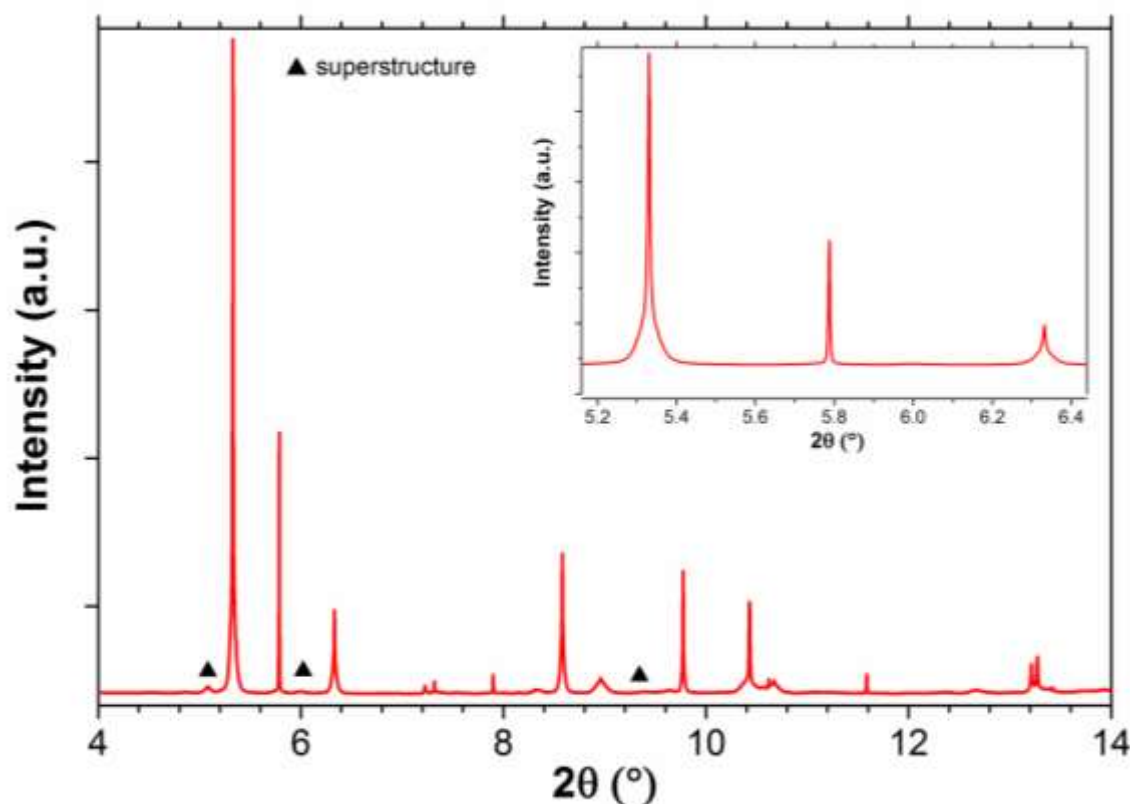


**Figure 1.** High resolution X-ray powder diffraction of  $\text{LaW}_x\text{Nb}_{1-x}\text{O}_{4+x/2}$  ceramics with  $x = 0.16$  collected at the temperature of 300 K. Peaks owing to the superstructure are marked with a triangle. The inset shows a few peaks near the main peak of the ceramics.

The biphasic nature of the sample and the additional peaks related to an incommensurate structure do not allow an accurate structural refinement with the Rietveld method to be performed. However, cell parameters at room temperature of the tetragonal phase can still be obtained by using the Le Bail method using GSAS [32] package with EXPGUI [33] interface. The resulting fit is reported in **Figure S2**. The lattice parameters of the tetragonal (scheelite) phase are  $a = 5.341(4) \text{ \AA}$ ,  $c = 11.6869(3) \text{ \AA}$  and  $V = 333.39(8) \text{ \AA}^3$ . The absence of clear peaks belonging to the sole monoclinic (fergusonite) phase does not allow a precise calculation of the cell parameters for this phase. Despite these values can be affected by a high error, a second Le Bail fit was performed with both tetragonal and monoclinic phases (**Figure S3**). The obtained cell parameters result in peak positions compatible with the asymmetry observed at the base of some diffraction peaks, i.e. at  $10.42^\circ 2\theta$  and  $9.6^\circ 2\theta$ , as can be observed in both **Figure S3** and **Figure S4**. Keeping in mind that these values should be affected by an error higher than reported by the software, the resulting parameters for the monoclinic phase are:  $a = 5.357(2) \text{ \AA}$ ,  $b = 11.688(2) \text{ \AA}$ ,  $c = 5.325(8) \text{ \AA}$ ,  $\beta = 90.49(9)^\circ$  and  $V = 333.4(8) \text{ \AA}^3$ . The suppression of the monoclinic distortion due to the introduction of tungsten is confirmed not only by the stabilisation of the tetragonal phase, but also by the significant decrease of the monoclinic angle  $\beta$  in comparison to the value of  $91.54^\circ$  reported for  $x = 0.12$  [34] and  $94.06^\circ$  in neat  $\text{LaNbO}_4$  [35].

### 3.2 XANES and EXAFS

The simulation of the W  $L_3$ -edge XANES spectra of a scheelite structure with composition  $\text{LaNb}_{0.84}\text{W}_{0.16}\text{O}_{4+\delta}$  is in very good agreement with the experimental data (plotted in red and black, respectively, **Figure 2**). In particular, the relatively sharp white line corresponding to the  $2p \rightarrow 5d$  transitions is an indication of tetrahedral  $\text{WO}_4$  coordination environment. The ligand field splitting depends on coordination, and leads to a broader double peak in  $\text{WO}_6$  octahedra: as shown in the inset of **Figure 2**, the double edge peak of  $\text{Cr}_2\text{WO}_6$  (where  $\text{W}^{6+}$  is octahedrally coordinated) arises from  $t_{2g}$ - $e_g$  splitting of the 5d states due to the octahedral coordination of oxygen atoms.

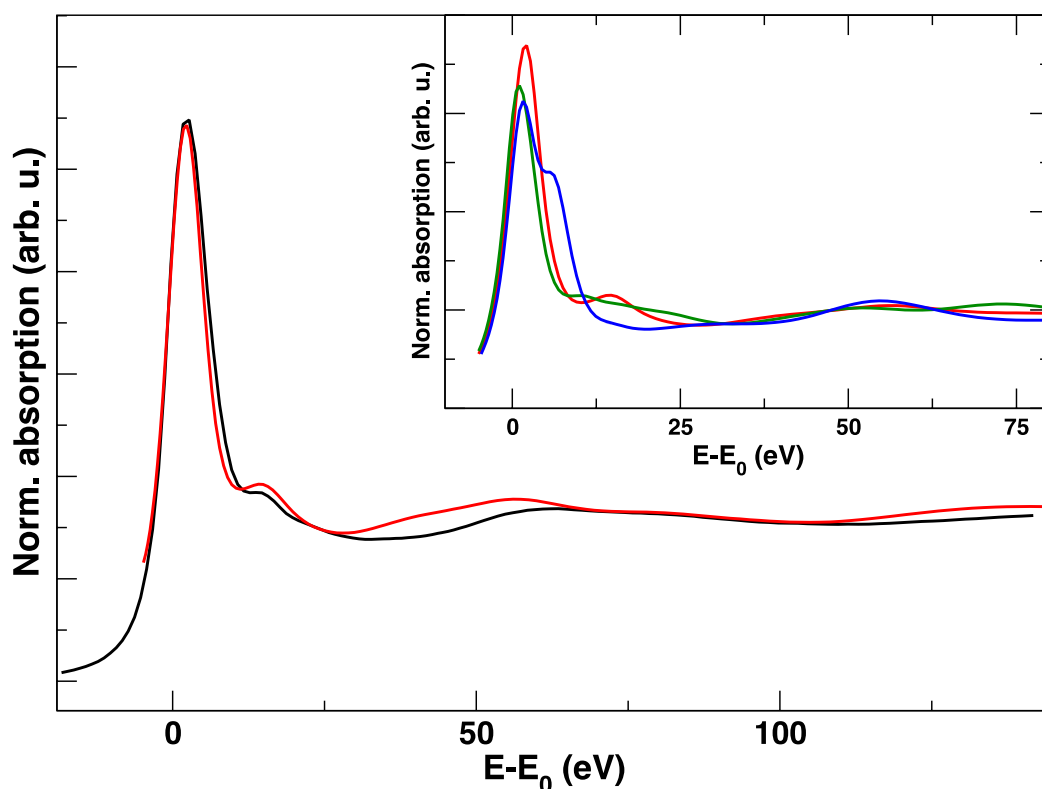


**Figure 2.** Normalised W L<sub>3</sub>-edge XANES spectrum of LWN (black) and simulated spectrum of a scheelite structure with LaNb<sub>0.84</sub>W<sub>0.16</sub>O<sub>4+δ</sub> composition (red). Inset: simulated XANES spectra of Na<sub>2</sub>WO<sub>4</sub> (green, tetrahedral coordination), Cr<sub>2</sub>WO<sub>6</sub> (blue, octahedral coordination), and LWN (red, tetrahedral coordination).

EXAFS analysis on bulk LWN reveals that tungsten is coordinated by 3.9(2) oxygen atoms placed at 1.84(1) Å, with a rather large disorder factor of 0.010(3) Å<sup>2</sup>. This model gives a very satisfactory fit of the first shell data (see **Figure 3** and **Figure 4**). The very short W-O distance is compatible with W<sup>6+</sup>-O<sup>2-</sup> bond. It can then be concluded that in LWN tungsten has +6 valence state, it replaces Nb<sup>5+</sup> in its site, and no other valence states (e.g. W<sup>5+</sup>) are present.

It is worth noting that the shells beyond the first (W-La etc.) are barely recognisable in the Fourier transform, indicating that the static disorder is very significant in the local environment of tungsten. This further corroborates the earlier observation of a high local disorder in the XRPD data.

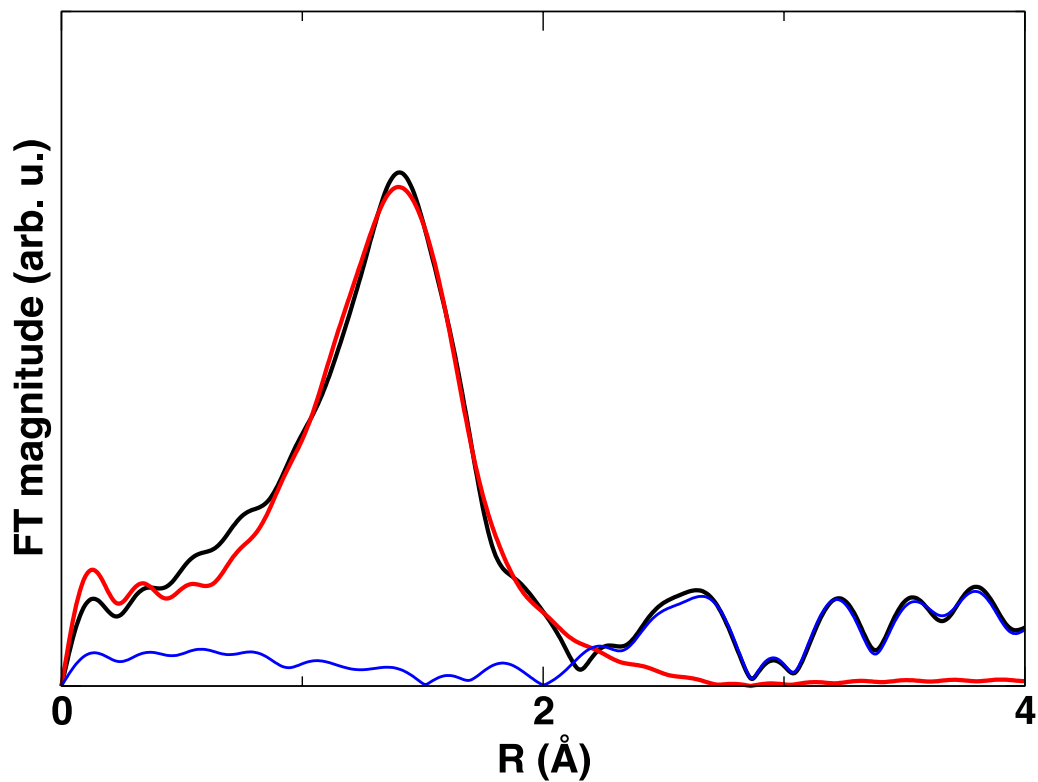


**Figure 3.** Magnitude of Fourier-transformed W L<sub>3</sub>-edge EXAFS data of LWN (black), best fitting (red) and residual (blue).

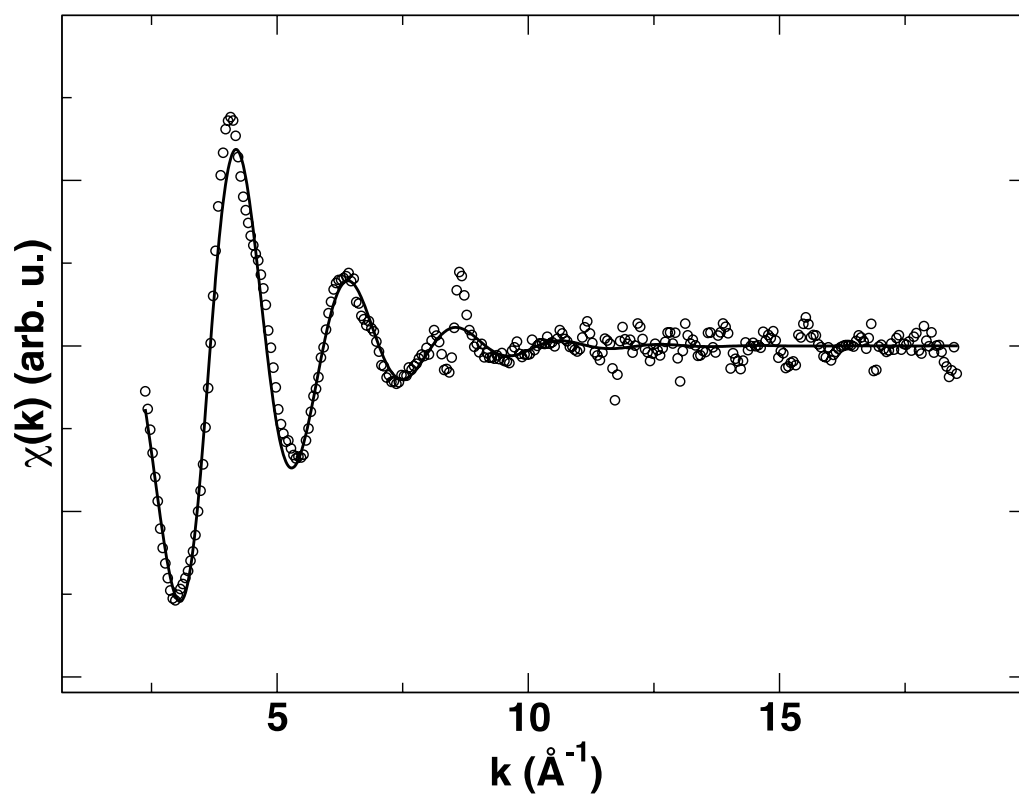


**Figure 4.** Experimental W L<sub>3</sub>-edge EXAFS data of LWN (circles) and best fitting (line).



### 3.3 X-ray microscopy on LSM-LWN diffusion couple

With the perspective of the use of LWN as electrolyte for SOFCs, a detailed investigation of its chemical compatibility with a potential cathode material was performed. During both processing and operation, in fact, the electrode and the electrolyte are in contact at a relatively high temperature. LSM has been already reported as the most compatible cathode material for both  $\text{LaNbO}_4$ , either neat [20] or Ca-doped [21,22], and LWN [13] and it has a thermal expansion coefficient, or CTE, of  $11.2 \cdot 10^{-6} \text{ K}^{-1}$  [36], similar to the one reported for the  $\text{LaNb}_{0.84}\text{W}_{0.16}\text{O}_{4.08}$  composition, i.e.  $14.5 \cdot 10^{-6} \text{ K}^{-1}$  [17], thereby reducing the possibility of mechanical failure. The electrode/electrolyte couple geometry used in the present study was chosen in order to maximise the contact between the two materials while maintaining a definite interface.

The concentration profiles reported in **Figure 5** were built from microXRF elemental maps, calculating the distance and concentration profiles perpendicularly to the electrode/electrolyte interface, thus compensating for eventual tilting of the interface respect to the scanning direction, by averaging in the horizontal direction over the widest available area, i.e. tens of microns. The LSM/LWN interface after prolonged thermal treatment at  $1150 \text{ }^\circ\text{C}$  for 72 h shows a remarkable alteration in the concentration profiles (**Figure 5**). In particular, the concentration profiles of strontium and niobium are smeared across the interface towards the other side: strontium in particular shows an appreciable concentration in LWN even around  $-10 \text{ }\mu\text{m}$ . Tungsten, on the other hand, accumulates on the LWN side close to the interface, before sharply decreasing in concentration in LSM. In particular, in the LWN regions closer to the interface (from  $-15$  to  $0 \text{ }\mu\text{m}$ ), the tungsten/niobium ratio goes from 0.4 to 0.6 (a 2/3-fold increase from the average starting composition). According to the  $\text{LaNbO}_4/\text{LaWO}_{4.5}$  phase diagram [16], such a tungsten enrichment in these regions is due primarily to a mixture of  $\text{LaW}_{0.22}\text{Nb}_{0.78}\text{O}_{4+x/2}$  and  $\text{LaW}_{0.60}\text{Nb}_{0.40}\text{O}_{4+x/2}$ . A smaller amount of scheelite-type  $\text{SrWO}_4$  may also form as a consequence of strontium diffusion, but quantitatively this phase is expected to be very minor due to the relatively low strontium concentration inside LWN.

On the LSM side, the  $0\text{-}20 \text{ }\mu\text{m}$  region is perturbed, showing an appreciable strontium depletion, and a slight lanthanum enrichment towards the interface. The presence of niobium on the LSM side is consistent with results on LSM and Ca-doped  $\text{LaNbO}_4$  annealed at  $1150 \text{ }^\circ\text{C}$  by Kravchyk et al. [22], who attributed the increase of LSM unit cell on annealed powder mixtures to the

niobium diffusion observed by SEM/EDS around the interface of an electrode/electrolyte bilayer, and it is in line with the formation of  $\text{LaCo}_{1-x}\text{Nb}_x\text{O}_3$  as a result of reactivity between  $\text{LaCoO}_3$  perovskite and  $\text{LaNbO}_4$  [20,37]. It is as well consistent with our previous results on  $\text{Ca:LaNbO}_4/\text{LSM}$  couples [23], where we observed that Nb adopted octahedral coordination after diffusion into the LSM side, which suggested its incorporation in the perovskite structure.

By closer inspection of the concentration maps (**Figure 6**), a few more observations can be made: 1) in the LWN region, there is an evident W/Nb anticorrelation, while La shows no correlations with either W nor Nb: these observations support again the existence of a two-phase system composed of W-doped  $\text{LaNbO}_4$  and Nb-doped  $\text{LaWO}_{4.5}$ ; the W/Nb anticorrelation is even more evident in specific areas of the LWN region with a strong enrichment of W and depletion of Nb; 2) after diffusing inside LWN, Sr does not accumulate in definite spots, suggesting that it is incorporated in lower concentration in the above phases substituting La; 3) a small amount of tungsten manages to diffuse in the LSM region, and around 10  $\mu\text{m}$  after the interface it clusters in very small clumps (less than 1  $\mu\text{m}$  in size); 4) the LSM bulk region shows some 2-3  $\mu\text{m}$  sized islets enriched in manganese and depleted in A-site cations, a feature already observed in the LSM/SDC couple [25] that disappeared with more prolonged thermal treatment. The accumulation of tungsten on the LWN side close to the interface and in small islets with size lower than a micron, together with the strontium diffusion into the LWN side is compatible with the presence of  $\text{SrWO}_4$  scheelite, in agreement with our previous results on powder mixtures annealed at 1200 °C [13]. Moreover, in Ref. [13] the splitting of the main peak in XRPD for LWN suggested the presence of a monoclinic distortion of LWN, indicating that after thermal treatment a depletion of W from LWN may take place.

Mn K-edge microXANES spectra were acquired in selected points in the vicinity of the LSM/LWN interface (**Figure 7**) to obtain information about its oxidation state and chemical environment. The overall shape of all spectra resembles that of bulk LSM, showing features that are typical of octahedrally coordinated Mn cations in a perovskite structure. In fact, spectra acquired in points 1 to 4 do not show evident changes. In point 5, acquired in the LWN region, a shift of the absorption edge about 3 eV towards lower energy is evident, along with a less pronounced pre-edge peak at 6540 eV. Both these changes are consistent with a lower oxidation state for Mn, and thus with a  $\text{LaMnO}_3$ -type perovskite phase formed by Mn after its diffusion in LWN [38], as already observed for other electrolytes ( $\text{Sm:CeO}_2$  and BCY) in combination with LSM [25]. While quantitatively such phase is certainly negligible, it proves

once more that the ability of Mn to adopt a variety of chemical states and environments drives the solid-state reactivity between Mn-containing electrodes and electrolyte materials.

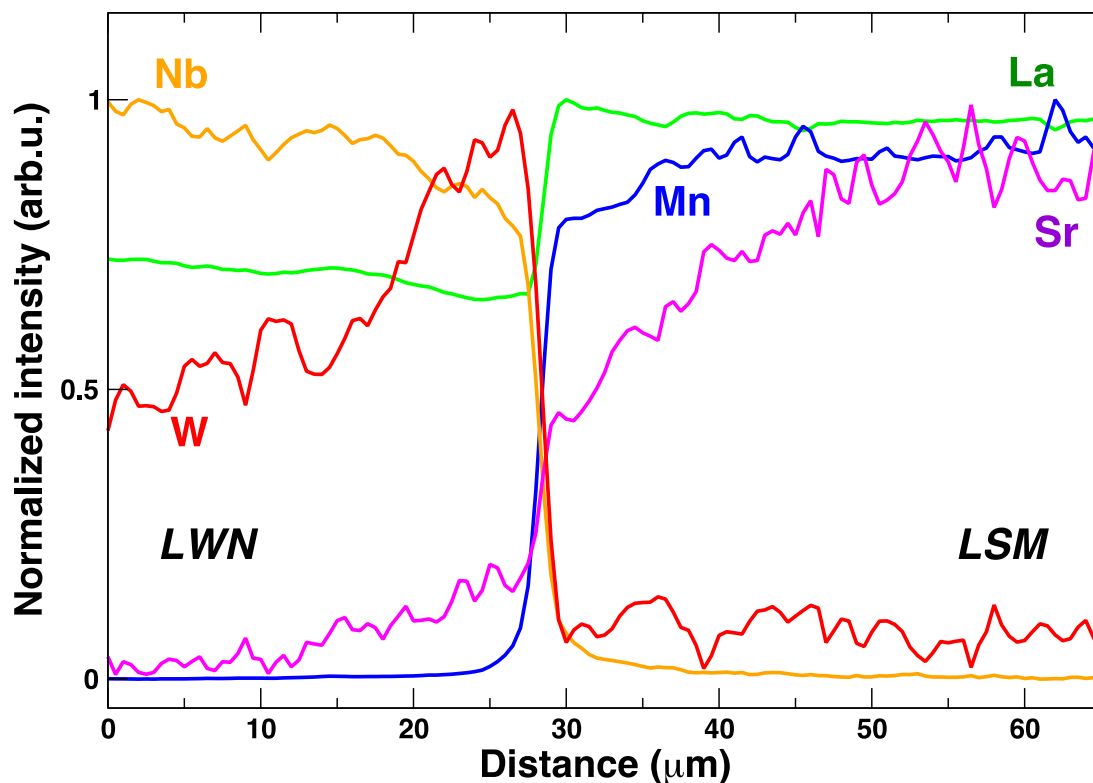


**Figure 5.** LSM/LWN interface at the Mn K-edge. Concentration profiles of lanthanum (green), niobium (yellow), tungsten (red), strontium (violet) and manganese (blue).

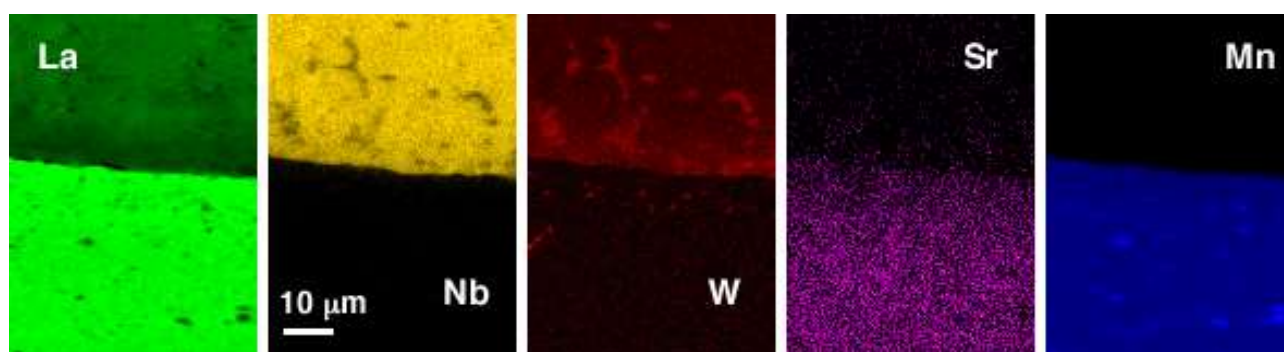


**Figure 6.** XRF maps of the LSM (bottom)/LWN (top) interface at the Mn K-edge. Left to right: concentration maps of lanthanum (green), niobium (yellow), tungsten (red), strontium (violet) and manganese (blue).

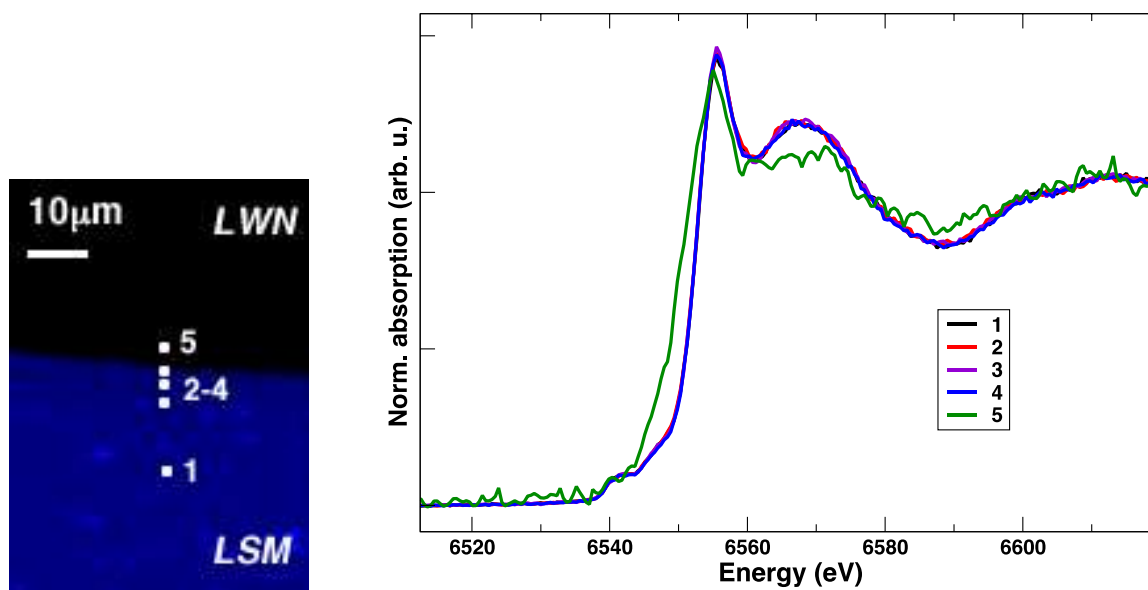


**Figure 7.** LSM/LWN interface at the Mn K-edge. (Left) concentration map of manganese (blue) with the spots where microXANES spectra were recorded. (Right) Mn K-edge microXANES spectra.

#### 4. Conclusions

The scheelite-type series  $\text{LaW}_x\text{Nb}_{1-x}\text{O}_{4+x/2}$  is attracting increasing interest due to its electrochemical properties compatible with almost pure oxide ion conductivity. Following our previous study on  $\text{LaW}_x\text{Nb}_{1-x}\text{O}_{4+x/2}$ ,  $x = 0.16$ , we focussed our investigation on the structural effect of tungsten insertion in the lattice with different synchrotron X-ray structural techniques. X-ray diffraction showed that the partial substitution of niobium with tungsten in the lattice in  $\text{LaW}_{0.16}\text{Nb}_{0.84}\text{O}_{4.08}$  stabilises the high temperature tetragonal structure, although not completely since the existence of a minor amount of monoclinic phase is indicated by the broadening of the tetragonal peaks near their base. The tungsten introduced in the lattice was proven to be in its 6+ oxidation state by XANES/EXAFS analysis, and no  $\text{W}^{5+}$  could be detected. As a possible electrolyte material for SOFCs, a detailed study of cation interdiffusion and eventual reactions at the interface is necessary: here, we addressed the issue with X-ray microspectroscopy with submicron resolution. We can conclude that LWN shows limited reactivity towards  $\text{La}_{0.8}\text{Sr}_{0.2}\text{MnO}_3$ , LSM after a prolonged thermal treatment at high temperature, which simulates the thermal treatment necessary during processing and prolonged operation of a real device. Clear but limited interdiffusion of cations was observed

in the present experimental conditions, with Sr depleting from the LSM side and diffusing into the LWN side, possibly forming a scheelite-type  $\text{SrWO}_4$  phase. In some areas within bulk LWN, the W to Nb ratio changes suggesting the formation of a two-phase system composed of W-doped  $\text{LaNbO}_4$  and Nb-doped  $\text{LaWO}_{4.5}$ ; a small fraction of manganese diffuses into LWN, maintaining however the octahedral coordination typical of the perovskite structure.

## Acknowledgements

This work was performed within the framework of the MIUR Project FIRB2012: "INCYPIT", Ref. RBFR12CQP5. The authors also acknowledge funding through MIUR projects PON R&C "TESEO" and PRIN "BIOITSOFC". We are grateful to the companies H.C. Starck and Treibacher Industrie AG, for providing some of the raw materials, to the ESRF for provision of beamtime, and we thank the staff of beamline ID21 and ID22 for assistance during the measurements. Dr. Wout De Nolf (ESRF) is acknowledged for useful discussions and assistance during data analysis.

## References

- [1] D.J.L. Brett, A. Atkinson, N.P. Brandon, S.J. Skinner, Intermediate temperature solid oxide fuel cells, *Chem. Soc. Rev.* 37 (2008) 1568–1578.
- [2] K.C. Wincewicz, J.S. Cooper, Taxonomies of SOFC material and manufacturing alternatives, *J. Power Sources* 140 (2005) 280–296.
- [3] A.J. Jacobson, Materials for solid oxide fuel cells, *Chem. Mater.* 22 (2010) 660-674.
- [4] A. Orera, P.R. Slater, New chemical systems for Solid Oxide Fuel Cells, *Chem. Mater.* 22 (2010) 675–690.
- [5] E. Fabbri, D. Pergolesi, E. Traversa, Materials challenges toward proton-conducting oxide fuel cells: a critical review, *Chem. Soc. Rev.* 39 (2010) 4355–4369.
- [6] A. Mielewczyk-Gryn, K. Gdula-Kasica, B. Kusz, M. Gazda, High temperature monoclinic-to-tetragonal phase transition in magnesium doped lanthanum ortho-niobate, *Ceram. Int.* 39 (2013) 4239–4244.

- [7] T. Mokkelbost, I. Kaus, R. Haugrud, T. Norby, T. Grande, M.-A. Einarsrud, High-temperature proton-conducting lanthanum ortho-niobate-based materials. Part II: Sintering properties and solubility of alkaline earth oxides, *J. Am. Ceram. Soc.*, 91 (2008) 879–886.
- [8] R. Haugrud, T. Norby, Proton conduction in rare-earth orthoniobates and orthotantalates, *Nat. Mater.* 56 (2006) 193.
- [9] E.V. Tsipis, C.N. Munnings, V.V. Kharton, S.J. Skinner, J.R. Frade, Transport properties and structural stability of tetragonal  $\text{CeNbO}_{4+\delta}$ , *Solid State Ionics* 177 (2006) 1015–1020.
- [10] T. Esaka, Ionic conduction in substituted scheelite-type oxides, *Solid State Ionics* 136–137 (2000) 1–9.
- [11] B.K. Maji, H. Jena, R. Asuvathraman, K.V. Govindan Kutty, Electrical conductivity and thermal expansion behavior of  $\text{MMoO}_4$  ( $M = \text{Ca, Sr and Ba}$ ), *Journal of Alloys and Compounds*, 640 (2015) 475–479.
- [12] A. Petrov, P. Kofstad, Electrical conductivity of  $\text{CaMoO}_4$ , *Journal of Solid State Chemistry* 30 (1979) 83–88.
- [13] G. Canu, V. Buscaglia, C. Ferrara, P. Mustarelli, S. Patricio, A.I.B. Rondao, C. Tealdi, F.M.B. Marques, Oxygen transport and chemical compatibility with electrode materials in scheelite-type  $\text{LaW}_x\text{Nb}_{1-x}\text{O}_{4+x/2}$  ceramic electrolyte, *Journal of Alloys and Compounds* 697 (2017) 392–400.
- [14] M.A. Laguna-Bercero, R.D. Bayliss, S.J. Skinner,  $\text{LaNb}_{0.84}\text{W}_{0.16}\text{O}_{4.08}$  as a novel electrolyte for high temperature fuel cell and solid oxide electrolysis applications, *Solid State Ionics* 262 (2013), 298–302.
- [15] C. Li, R.D. Bayliss, S.J. Skinner, Crystal structure and potential interstitial oxide ion conductivity of  $\text{LnNbO}_4$  and  $\text{LnNb}_{0.92}\text{W}_{0.08}\text{O}_{4.04}$  ( $\text{Ln} = \text{La, Pr, Nd}$ ), *Solid State Ionics* 262 (2014) 530–535.
- [16] R.J. Cava, R.S. Roth, T. Negas, H.S. Parker, D.B. Minor, Crystal chemistry, modulated structure, and electrical conductivity in the oxygen excess scheelite-based compounds  $\text{La}_{1-x}\text{Th}_x\text{NbO}_{4+x/2}$  and  $\text{LaNb}_{1-x}\text{W}_x\text{O}_{4+x/2}$ , *Journal of Solid State Chemistry* 40 (1981) 318.
- [17] C. Li, S.S. Pramana, R.D. Bayliss, C.P. Grey, F. Blanc, S.J. Skinner, Evolution of structure in the incommensurate modulated  $\text{LaNb}_{1-x}\text{W}_x\text{O}_{4+x/2}$  ( $x = 0.04\text{--}0.16$ ) oxide ion conductors, *Chem. Mater.* 32 (2020) 2292–2303.

- [18] C. Ferrara, A. Mancini, C. Ritter, L. Malavasi, C. Tealdi, Interstitial oxide ion migration in scheelite-type electrolytes: a combined neutron diffraction and computational study, *Journal of Materials Chemistry A* 3 (2015) 22258–22265.
- [19] K. Toyoura, Y. Sakakibara, T. Yokoi, A. Nakamura, K. Matsunaga, Oxide-ion conduction via interstitials in scheelite-type  $\text{LaNbO}_4$ : a first-principles study, *J. Mater. Chem. A* 6 (2018) 12004.
- [20] J.R. Tolchard, H.L. Lein, T. Grande, Chemical compatibility of proton conducting  $\text{LaNbO}_4$  electrolyte with potential oxide cathodes, *J. Eur. Ceram. Soc.* 29 (2009) 2823–2830.
- [21] A. Magrasó, M.-L. Fontaine, R. Bredesen, R. Haugrud, T. Norby, Cathode compatibility, operation, and stability of  $\text{LaNbO}_4$ -based proton conducting fuel cells, *Solid State Ionics* 262 (2014) 382–387.
- [22] K.V. Kravchyk, E. Quarez, C. Solís, J.M. Serra, O. Joubert, Cathode materials for  $\text{La}_{0.995}\text{Ca}_{0.005}\text{NbO}_4$  proton ceramic electrolyte, *Int. J. Hydr. En.* 36 (2011) 13059–13066.
- [23] F. Giannici, G. Canu, M. Gambino, A. Longo, M. Salomè, M. Viviani, A. Martorana, Electrode-electrolyte compatibility in Solid-Oxide Fuel Cells: Investigation of the LSM-LNC interface with X-ray microspectroscopy, *Chemistry of Materials* 27 (2015) 2763–2766.
- [24] F. Giannici, G. Canu, A. Chiara, M. Gambino, C. Aliotta, A. Longo, V. Buscaglia, A. Martorana, Cation diffusion and segregation at the interface between samarium-doped ceria and LSCF or LSCu cathodes investigated with X-ray microspectroscopy, *ACS Appl. Mater. Interfaces* 9 (2017) 44466–44477.
- [25] F. Giannici, A. Chiara, G. Canu, A. Longo, A. Martorana, Interface solid-state reactions in  $\text{La}_{0.8}\text{Sr}_{0.2}\text{MnO}_3/\text{Ce}_{0.8}\text{Sm}_{0.2}\text{O}_2$  and  $\text{La}_{0.8}\text{Sr}_{0.2}\text{MnO}_3/\text{BaCe}_{0.9}\text{Y}_{0.1}\text{O}_3$  disclosed by X-ray microspectroscopy, *ACS Appl. Energy Mater.* 2 (2019) 3204–3210.
- [26] A. Fitch, The High Resolution Powder Diffraction Beam Line at ESRF, *J. Res. Natl. Inst. Stand. Technol.* 109 (2004) 133.
- [27] O. Bunau, Y. Joly, Self-consistent aspects of x-ray absorption calculations, *J. Phys.: Condens. Matter* 21 (2009) 345501.
- [28] K.D. Klementev, Extraction of the fine structure from x-ray absorption spectra, *J. Phys. D: Appl. Phys.* 34 (2001) 209.
- [29] J.J. Rehr, J.J. Kas, F.D. Vila, M.P. Prange, K. Jorissen, Parameter-free calculations of x-ray spectra with FEFF9, *Phys. Chem. Chem. Phys.*, 12 (2010) 5503–5513.

- [30] M. Salome, M. Cotte, R. Baker, R. Barrett, N. Benseny-Cases, G. Berruyer, D. Bugnazet, H. Castillo-Michel, C. Cornu, B. Fayard, E. Gagliardini, R. Hino, J. Morse, E. Papillon, E. Pouyet, C. Rivard, V.A. Sole, J. Susini, G. Veronesi, The ID21 Scanning X-ray Microscope at ESRF, *J. Phys.: Conf. Ser.* 425 (2013) 182004.
- [31] V.S. Stubican, High temperature transitions in rare-earth niobates and tantalates, *J. Am. Ceram. Soc.* 47 (1964) 55–58.
- [32] A.C. Larson, R.B. Von Dreele, GSAS - General Structure Analysis System, LAUR 86–748 (1994).
- [33] B.H. Toby, EXPGUI, a graphical user interface for GSAS, *J. Appl. Cryst.* 34 (2001) 210–213.
- [34] C. Li, S.S. Pramana, S.J. Skinner, Room temperature structure and transport properties of the incommensurate modulated  $\text{LaNb}_{0.88}\text{W}_{0.12}\text{O}_{4.06}$ , *Dalton Trans.* 48 (2019) 1633.
- [35] M. Huse, A.W.B. Skilbred, M. Karlsson, S.G. Eriksson, T. Norby, R. Haugrud, C.S. Knee, Neutron diffraction study of the monoclinic to tetragonal structural transition in  $\text{LaNbO}_4$  and its relation to proton mobility, *J. Solid State Chem.* 187 (2012) 27–34.
- [36] Y. Sakaki, Y. Takeda, A. Kato, N. Imanishi, O. Yamamoto, M. Hattori, M. Iio, Y. Esaki,  $\text{Ln}_{1-x}\text{Sr}_x\text{MnO}_3$  (Ln=Pr, Nd, Sm and Gd) as the cathode material for solid oxide fuel cells. *Solid State Ionics* 118 (1999) 187–194.
- [37] V. Øy garden, H.L. Lein, T. Grande, Structure, thermal expansion and electrical conductivity of Nb-substituted  $\text{LaCoO}_3$ , *J. Solid State Chem.* 192 (2012) 246–254.
- [38] J. Chaboy, Relationship between the structural distortion and the Mn electronic state in  $\text{La}_{1-x}\text{Ca}_x\text{MnO}_3$ : a Mn *K*-edge XANES study, *J. Synchrotron Rad.* 16 (2009) 533–544.